TABLE VIII. Results for $Zr^{91}(d,t)Zr^{90}$ reactions. The spins and parities of the final states (of Zr^{90}) are known from other sources. The X indicates the ratio of the normalization for the unknown l of the 2.77-MeV state to that of $l=2$.

$E(d,t)$	I_f	$\sigma(d,t)$ (mb/sr)	S'	Proton configuration
0	0^+	0.95	1.00	$(0.75)^{1/2}p_{1/2}{}^2+(0.25)^{1/2}g_{9/2}{}^2$
1.75	0^+	0.004	0.005	$(0.25)^{1/2}p_{1/2}{}^2-(0.75)^{1/2}g_{9/2}{}^2$
2.21	2^+	0.036	0.055	$(g_{9/2})^2$
2.77	3^-	0.041	$0.066X$	

creasing the normalization for $l=2$ (d,t) reactions in the other zirconium isotopes by 5.5%; for example, the number of $d_{5/2}$ particles in Zr^{96} would be reduced from 5.75 to 5.44 ($\pm10\%$ in each case).

Another possible explanation for the (d,t) reaction to the 2.21-MeV state is to assume that it contains a fraction f of $(d_{5/2}g_{9/2}{}^{-1})$ in its neutron configurations and that the reaction proceeds by $g_{9/2}$ pickup. This

would increase S' by a factor of 4, whence it would require $f\simeq0.22$. This is unexpectedly large.

The most likely explanation for the excitation of the 2.77-MeV level is that its configuration contains a fraction of F of $(d_{5/2}p_{1/2}{}^{-1})$, so that the process proceeds by a pickup of a $p_{1/2}$ neutron. One then expects $X\simeq\frac{1}{2}$, so that $F\simeq3\%$.

However, in view of the difficulties discussed in Sec. VI, judgment should perhaps be reserved on any conclusions from weak transitions in (d,t) reactions.

Elastic Scattering of 1.2-BeV/c Muons from Hydrogen*

H. F. Davis, T. E. Ewart, G. E. Masek, E. D. Platner, J. P. Toutonghi, and R. W. Williams

Department of Physics, University of Washington, Seattle, Washington

(Received 8 April 1963)

The absolute cross section for the elastic scattering of negative muons from protons was measured over a range of momentum transfers of 450 to 850 MeV/c. The muon beam was formed by decay in flight of Bevatron produced pions and was separated from the pion beam electronically by using four gas-filled threshold Čerenkov counters. A total of 3×10^8 muons were incident on two large liquid hydrogen targets in tandem and gave a total of 56 ± 9 acceptable scattering events, as compared to 48 predicted by the Rosenbluth formula for electromagnetic scattering from protons. A χ-square analysis of the scattered events gave agreement at the 75% level for the angular distribution of the data and the theoretical predictions, and gave with 95% confidence $\Lambda^{-1}\leq0.16$ F, where Λ^{-1} is the conventional breakdown parameter. Hence, in this experiment, the behavior of muons scattered from protons at large momentum transfers is indistinguishable from that of electrons.

I. INTRODUCTION

THE high-energy scattering of muons in nuclear matter has been the object of many experimental investigations with the hope of uncovering a fundamental difference between muons and electrons. Prior to about 1958 these investigations showed a wide range of results with respect to the appropriate form of the electromagnetic cross section and there appeared to be a strong possibility that a large anomaly existed in the muon interaction, which might be due to a non-electromagnetic interaction or a breakdown in quantum electrodynamics for the muon.[1] Since 1958 several new

experiments have been done with both cosmic-ray and accelerator-produced muons.[2-8] These experiments have covered a wide range of incident muon energies (20–2000 MeV) and momentum transfers (20–400 MeV/c), and have used various target nuclei (carbon, lead, and nuclear emulsions). With one exception,[8] they have all

[1] For a summary of high-energy muon experiments prior to 1958 see G. N. Fowler and A. W. Wolfendale, Progr. Elem. Particle Cosmic Ray Phys. 4, 123 (1958).

[2] S. Fukui, T. Kitamura, and Y. Watase, Phys. Rev. 113, 315 (1959).

[3] G. E. Masek, L. D. Heggie, Y. B. Kim, and R. W. Williams, Phys. Rev. 122, 937 (1961).

[4] C. Y. Kim, S. Kaneko, Y. B. Kim, G. E. Masek, and R. W. Williams, Phys. Rev. Letters 122, 1641 (1961).

[5] P. L. Connelly, J. G. McEwen, and J. Orear, Phys. Rev. Letters 6, 554 (1961).

[6] D. Kotelchuck, J. G. McEwen, and J. Orear, Phys. Rev. 129, 876 (1963).

[7] A. Citron, C. Delorme, D. Fries, L. Goldjahl, J. Heitze, G. E. Michaelis, C. Richard, and H. Øverås, Phys. Letters 1, 175 (1962).

[8] R. L. Sen Gupta, S. Gosh, A. Acharya, M. M. Biswas, and K. K. Roy, Nuovo Cimento 19, 245 (1961).

found good agreement with the appropriate electromagnetic cross sections. Hence, the question of the existence of a large muon scattering anomaly now appears to be settled; no such anomaly exists.

It is important to the understanding of elementary particles to extend the investigations on possible muon-electron differences. For elastic muon scattering there are two dynamical relativistic invariants, the total center-of-mass energy, and the four-momentum transfer, and one might expect to see such differences occurring either at large momentum transfer (for which specific models have been proposed[9]) or high energy or both.

The experiment described[10] here is a measurement of the cross section for the elastic scattering of muons from free protons at momentum transfers between 450 and 850 MeV/c (5–18 F^{-2}) and at an average incident momentum of 1.21 BeV/c. Liquid hydrogen was used for the target material to avoid the difficulties of theoretical interpretation which exist with complex nuclei. The small cross sections (10^{-29}–10^{-31} cm^2/sr) and low beam intensities ($\sim$1000 muons/sec) necessitated the use of a very large scattering target and a large solid angle scattering detector. For the target, we used two liquid hydrogen targets (each 54 in. long and 9 in. in diameter) and the detectors were spark chambers which had azimuthal efficiency of about 20%. In addition to the problem of low yield, the experiment had to contend with the effects of a large pion contamination. The muon beam actually contained more pions than muons ($\sim$4:1). The pion-proton elastic scatterings were kinematically indistinguishable from the muon scatterings in our spark chambers and the pion cross section was $\sim$10^4 times larger. A series of four gas Čerenkov counters was employed to electronically eliminate the pions and give an effective rejection of about 10^6. To measure the rejection (and, hence, the final pion background in our scattering distribution) we rely upon the difference in the angular distribution between elastically scattered muons and pions, as there are proportionately many more large-angle pion scatterings. A total of 3×10^8 incident muons yielded 78 elastically scattered events

between 22° and 45°. The total number and angular distribution agree well with the theoretical Rosenbluth cross section using the form factors measured by electron scattering.
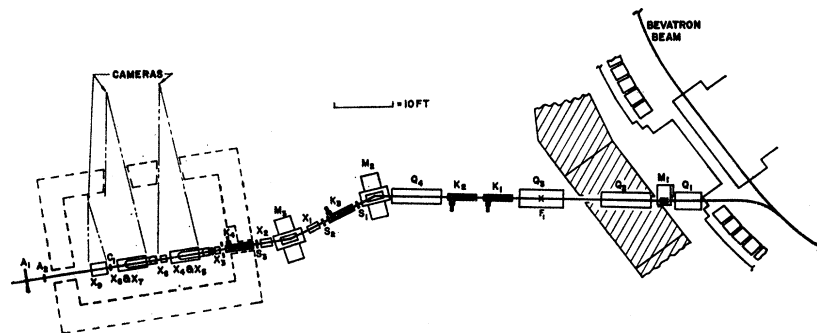
II. EXPERIMENTAL ARRANGEMENT

1. General

A 1.2 BeV/c beam consisting predominantly of pions ($\sim$80%) and muons ($\sim$20%) was used as the muon source. This beam passed through a system of magnets and gas Čerenkov counters (Fig. 1), which electronically selected the muons and rejected the pions, and then was directed onto the two liquid hydrogen targets arranged in tandem. A system of scintillation counters was placed around the targets to select events in which a scattered muon and its recoil proton emerged (Fig. 2). This counter system triggered a set of three spark chambers which allowed observation of the incident muon trajectory into the target and the scattered muon and recoil proton trajectories from the target. Provisions were also made to measure the incident momentum of each scattered muon by another system of spark chambers (X_1 and X_2 of Fig. 1), and to identify which of the outgoing particles was the muon.

2. Beam

The beam originated from an internal Bevatron target located in the curved section upstream of the West Tangent area. The quadrupoles Q_1 and Q_2 provided a vertical and horizontal focus of the target at F_1 (F_1 is located at the center of Q_3 in Fig. 1). The beam up to F_1 consisted predominantly of pions directly from the internal target and muons from pion decays in flight in the immediate vicinity of the target and along the beam channel. Attempts were made to physically separate the pions from the muons by placing at F_1 an absorber which was large compared to the vertical image but small compared to the total vertical aperture. The pions originating from a small object (the internal target) should preferentially strike the absorber, while

FIG. 1. Experimental arrangement of muon and pion beam. Quadrupoles Q_1 and Q_2 provided a vertical and horizontal focus at F_1 in the center of Q_3 which serves as a field lens. Bending magnets M_1, M_2, and M_3 selected 1.2-BeV/c particles. Čerenkov counters K_1, K_2, K_3, and K_4 selected the proper velocity for 1.2-BeV/c muons. Scintillators S defined the geometry of the beam and X were the spark chamber detectors. A detailed drawing of the scattering area is shown in Fig. 2.

[9] S. D. Drell, Ann. Phys. (N. Y.) 4, 75 (1958).
[10] A brief preliminary report of the work has already been published: G. E. Masek, T. E. Ewart, J. P. Toutonghi, and R. W. Williams, Phys. Rev. Letters 10, 35 (1963).
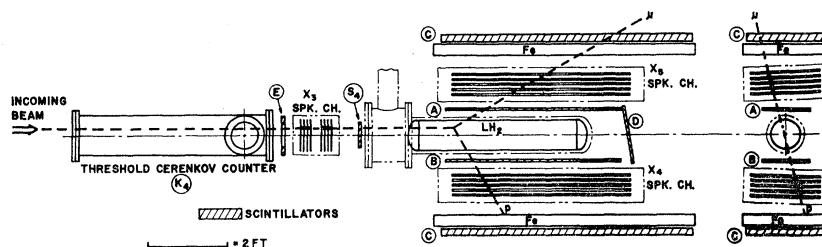
FIG. 2. Experimental arrangement of scattering area. The end of the beam defining equipment is shown as the last Čerenkov counter, K_4, and the beam defining spark chamber X_3. Not shown in this figure is the translation of X_3 by mirrors which can be seen in Fig. 12. To the right are the end views of the scattering chambers X_4 and X_5 seen by means of mirrors. The chambers were tilted to give the camera a better coverage of the gaps in the front view. A scattering event is drawn in, showing elastic kinematics in X_3, X_4, and X_5; also shown is the absorption of the proton and penetration of the muon which is essential for all events with a momentum transfer smaller than 800 MeV/c.

the muons, coming from an effectively larger object, should pass over and under the absorber. However, it proved impossible to obtain significant separation without reducing the absolute muon flux to unusable levels, and the method was abandoned. A field lens, Q_3, was placed at F_1 and the beam was directed onto the M_2 and M_3 magnet system.

A significant amount of physical separation was obtained by detuning the magnet M_1. The setting of M_1 which optimized the pion flux gave a muon to pion ratio of about 3% at the hydrogen targets. However, setting the current of M_1 15% lower increased the muon to pion ratio to about 25%, while keeping the absolute muon flux essentially the same. Thus, for the scattering runs the muon flux incident on the first target was about 4000 muons per burst and the muon to pion ratio was about 25%, giving a total flux (muons and pions) of about 20 000 per burst.

The magnet M_3 and the spark chambers X_1 and X_2 provided a means of measuring the momentum of individual beam particles. During the scattering runs these
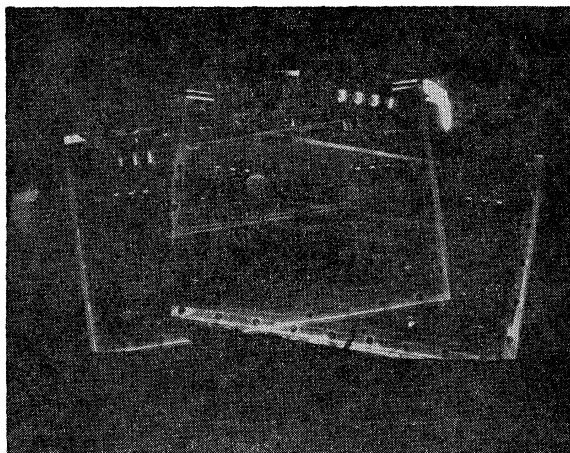

FIG. 3. Momentum defining photograph. A typical photograph of the X_1X_2 tracks superimposed on a single frame is shown. The angular difference between the two tracks uniquely defines the momentum for any fixed current setting of the bending magnet.

chambers were triggered whenever a scattering event occurred, and hence, gave the incident momentum of each scattered particle. In addition, runs were made to ascertain the momentum distribution of the incident beam, in which case X_1-X_2 were triggered on random incident muons. X_1 and X_2 were viewed from above by a single camera located on the top of M_3. A system of mirrors translated the two images to overlapping positions on the film from which a direct measurement of the bend angle could be made as the difference between the incoming and outgoing directions. (Figure 3 shows an X_1 and X_2 picture of an incident particle.) With this system the momentum of a beam particle could be measured to 2%.

3. Čerenkov Counter System

As mentioned above, one of the most difficult aspects of this experiment was to reduce the "effective" pion contamination in the beam and to demonstrate that it had been reduced. The elastic pion-proton scattering cross section in the kinematic regions of this experiment was about 10^4 times larger than the elastic muon cross section. Recalling that the pion-muon ratio in the beam was 4:1, we see that a pion reduction of about 10^6 was necessary to keep the pion scatterings to less than 10% of the muon scatterings. This was done electronically with the use of four gas threshold Čerenkov counters.[11] The rejection properties of a single Čerenkov counter can be seen from Fig. 4(a). The pions and muons in the beam have been momentum selected and, hence, have different velocities. One can adjust the pressure (index of refraction) of a gas counter so that the higher velocity muons give off Čerenkov radiation and the lower velocity pions do not. In practice, a fraction of the pions can still count via the mechanism of knock-on electrons, and this sets the single counter rejection rate. Figure 4(a) shows a pressure curve of one of our counters. At the high-pressure end, above both muon and pion counter thresholds, the ratio T_1CT_2/T_1T_2 (see Fig. 4

[11] The counters were each 60 in. long and 12 in. in diameter and were filled with SF$_6$. Their design was previously described. R. G. Swanson and G. E. Masek, Rev. Sci. Instr. 32, 212 (1961).
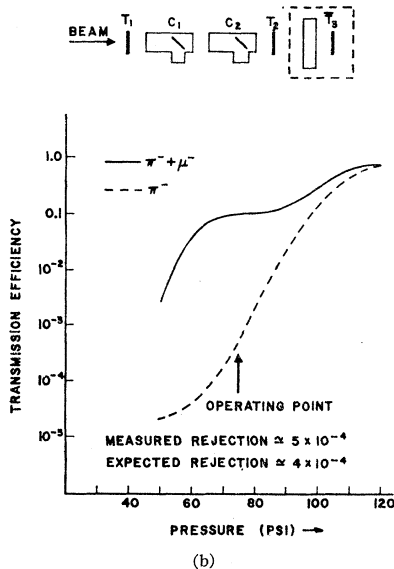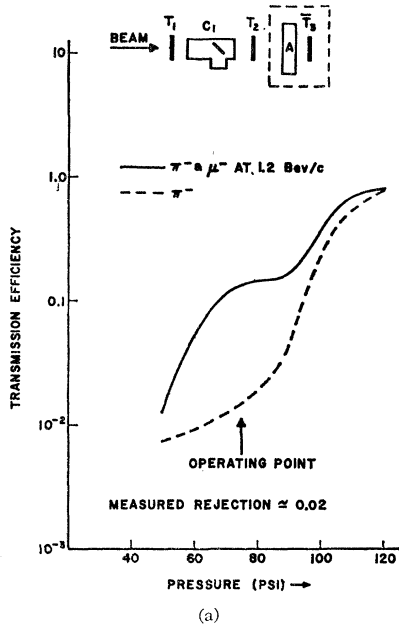
(a)

(b)

FIG. 4. (a) Experimental pressure curves for a single Čerenkov counter. For the solid curve, the transmission efficiency is the ratio of the particles that count in the Čerenkov counter to those incident, $T_1C_1T_2/T_1T_2$. For the dashed curve the transmission efficiency is the ratio of particles that count in the Čerenkov counter and which stop in the absorber to those which stop in the absorber, $T_1C_1T_2\bar{T}_3/T_1T_2\bar{T}_3$. The dashed curve was normalized to agree with the solid one at 120 psi. (b) Experimental pressure curves for two Čerenkov counters in series. The efficiency for pions (1.2 BeV/c) is about 5×10^{-4}; that is slightly larger than the square of a single counter efficiency $(0.02)^2=4\times10^{-4}$, showing that the counters were almost independent.

caption) tends toward 1. As the pressure is lowered below pion threshold the ratio drops and then tends to plateau at about 0.25 where one is counting predominantly muons. Below the muon threshold the ratio drops again to a value of about 0.02 and again tends to

plateau. This lower level is due to the knock-on electrons. To get the effective rejection of a single counter for the scattering experiment one must measure this knock-on rate at the muon operating pressure (about 75 psi). This was done by employing absorber A [see Fig. 4(a)] and requiring that particles stop in A. Thus, muons are rejected since they interact weakly and one is looking at knock-ons from pions that stop in A. The dashed curve of Fig. 4(a) shows a pressure curve under these conditions—the rejection is now the ratio of $T_1CT_2\bar{T}_3/T_1T_2\bar{T}_3$ at the muon operating pressure and is seen to be ~0.02. (This also agrees with the calculated value for the knock-on rate.) Thus, a single counter does not provide the necessary rejection for the experiment.

The rejection of a cascaded set should be the product of the individual counter rejections, providing there are no correlations between the knock-on electrons. To insure independence of the counters, they were arranged with magnets between them (except for K_1 and K_2). Knock-ons made in one counter would then be swept out by the magnetic fields, preventing them from entering the next counter. The rejection of two counters was measured in a manner analogous to that described for the single counter. The results of this measurement are shown in Fig. 4(b), and it is seen that $T_1C_1C_2T_2\bar{T}_3/T_1T_2\bar{T}_3$ at the muon operating pressure is about 5×10^{-4}, or approximately the square of the single counter rejection. No attempts were made to measure the rejection of 3 or 4 Čerenkov counters by this method, for already with the two counter measurement there is evidence of muons breaking through the anticoincidence. Instead, as described in Sec. III, the over-all pion contamination was measured using the scattered angular distribution.

4. Scattering Detector

The general arrangement of the end of the beam, the first hydrogen target, and its scattering detector are shown in Fig. 2 including an illustration of a typical scattering event. To trigger the spark chambers a particle had to go up the beam channel to the first hydrogen target which would be indicated by the fourfold coincidence, $S\equiv S_1S_2S_3S_4$, and it had to give the muon signature in the four Čerenkov counters $K\equiv K_1K_2K_3K_4$. An acceptable scattering event was characterized by a scattering particle (e.g., a muon) and its recoil proton counting in the scintillators A and B, and the scattering particle then penetrating the 70 g/cm^2 of iron and counting in C. The trigger is then $SKABC$. In addition (for reasons which will be discussed below), it was required that there be no count in scintillators E and D, so the final front target trigger was $SKABC\bar{D}\bar{E}$.

The back target and detector arrangement was almost identical to that of the front target and again the spark chambers would be triggered by $S'K\bar{A}'B'\bar{D}'\bar{E}'E$, where the primes indicate counters associated with the back target and $S'\equiv S_1S_2S_3S_5$. (There is an additional anti-
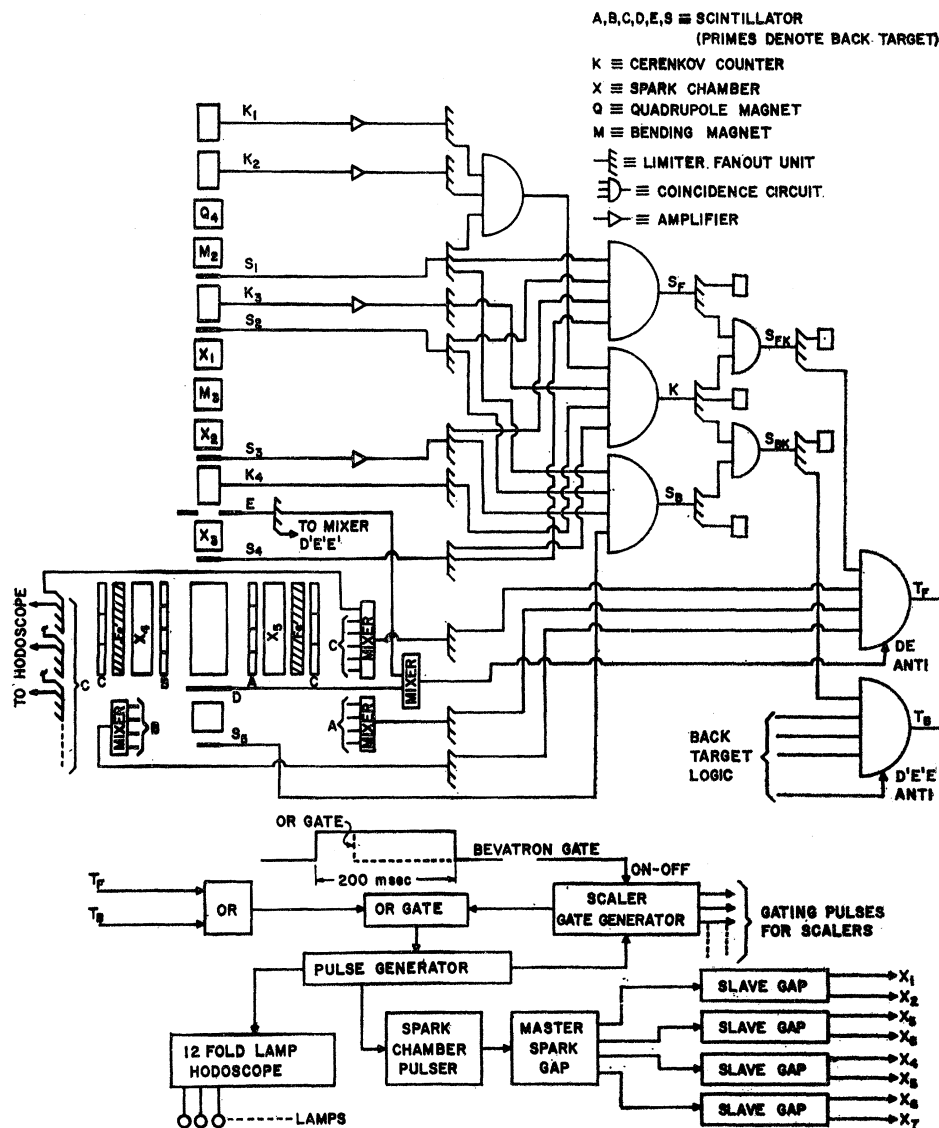
FIG. 5. Electronic block diagram. An output pulse from the last stage coincidence of either target electronics, T_F or T_B, indicates that a scattering event has occurred and has fulfilled all the triggering requirements. For example, a pulse out of T_F indicates a coincidence-anticoincidence logic of, $S_F K A B C \bar{E} \bar{D}$. The scalers are gated "on" by the Bevatron gate through the "Scaler Gate Generator" for the duration of the spill ($\sim$200 msec) unless T_F or T_B record a scattering event. The output of T_F or T_B through the "OR" circuit causes the Scaler Gate Generator to gate the scalers "off" until the next Bevatron burst, thus eliminating the need for dead-time corrections. The "OR" circuit also provides a pulse for triggering the spark-chambers and is then gated off.

coincidence $\bar{E}$ required here, see below.) In practice, a trigger from either the front target or the back target systems triggered all the spark chambers, X_1 through X_8, as is indicated by the electronics block diagram, Fig. 5.

To identify the penetrating particle,[12] a hodoscope was employed. The counter C was made up of six separate scintillators, three above the top iron absorber and three below the bottom absorber. A particle passing through any one of the C counters would light one of six lights associated with the respective counter. These

lights were arranged near the spark chambers so that they could be recorded on the same film as the spark chamber picture. In Fig. 12, which shows a typical event picture, the light can be seen near the arrow.[13]

5. Spark Chambers

A trigger from either the front target or back target would pulse all eight spark chambers. Three separate cameras were used to photograph the event, and the event number was displayed by means of Nixie lights on each film, thus, guaranteeing proper identification of the event on all three films. The first camera, as mentioned above, observed the top view of X_1 and X_2 and

---

[12] For elastic scatterings less than 45°, the momentum of the recoil proton was too low to allow penetration through the 70 g/cm² of iron. For angles greater than 45°, both the scattered and recoil particle can penetrate. Kinematics enables one to distinguish the muon in this case. For pion scattering the probability of large-angle scatters is high, and penetration of both particles was observed frequently in pion runs.

[13] The hodoscope gave good operation, free from pickup from the spark chamber high-voltage pulses. This circuit is described elsewhere.
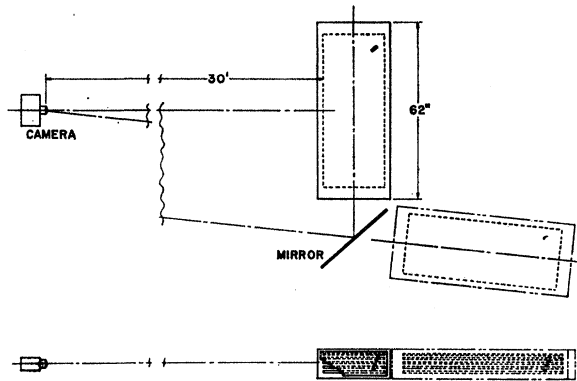
FIG. 6. Scattering chamber optics. As previously shown the spark chambers were tilted toward the camera. This figure shows the location of the camera axis with respect to the front view and the image at the end view of the chambers. A possible track is included.

measured the incident momentum of each event. The second camera viewed the front target and its detectors, while the third viewed the back target system. The latter cameras were located 30 ft from the targets (see Fig. 1) and photographed directly the front view of X_3, X_4, and X_5 (X_8, X_6, and X_7 for the back target), avoiding the use of field lenses. To permit the best coverage of all gaps, the chambers X_4 and X_5 were tilted towards the camera. The end views were observed through a single mirror which was adjusted so that the normal to the image of the end window at its center passed through the camera (Fig. 6). Again, no field lenses were employed for this view, and sparks near the rear of the chamber were actually seen via their reflection in the spark chamber plates (which were good specular surfaces of stretched aluminum foil). The image of X_3 was translated to the middle of the target by a system of mirrors to reduce the over-all image length on the film, and to bring it closer to the optical axis of the camera.

The scattering chambers X_3, X_4, X_5, and X_6 were all identical. The chamber plates were made by stretching 0.003-in. aluminum foil on a 24-in. by 60-in. frame formed from aluminum bar 1 in.$\times 1\frac{1}{2}$ in. in cross section.[14] Each chamber contained five of these frames arranged on an internal support, within a gas-tight box, to give four gaps of $\frac{3}{8}$-in. spacing. These chambers provided a measured angular accuracy of about 0.6°, nearly independent of track angle up to angles as large as 65° from the normal. The chambers X_1, X_2, X_3, and X_8 were of similar construction, but the plates were grouped into two separated 4 plate sets to provide greater angular resolution with a minimum number of gaps. Also, the gap spacing was $\frac{1}{4}$ in. in these chambers. All chambers were filled with 1 atm of argon which was bubbled through alcohol.

[14] David Nygren, Rev. Sci. Instr. **33**, 252 (1962).

6. Additional Electronic Notes

The high voltage pulses to the spark chambers were obtained from a system of triggered spark gaps (see Fig. 5). A central three-electrode spark gap gave simultaneous 20-kV pulses to four cylindrical two-electrode slave spark gaps. To minimize the lead inductance to the spark chambers the slave gaps were located as close as possible (a few feet) to the chambers they pulsed, and the high-voltage pulses were delivered via RG-8U cable. The operating voltage for the scattering chambers was 27 kV, and for the smaller chambers 20 kV. A gating provision is also shown in Fig. 5, which gates off the high-voltage trigger and all recording scalers after the spark chambers are triggered till the end of the Bevatron pulse. Thus, the scalers do not record flux during the dead time of the spark chambers and dead-time corrections do not have to be applied to the measured fluxes. The system is restored on the next Bevatron pulse. The triggering rate during the muon runs was about 1 in 100 000 muons, or once every 30 pulses, hence, no appreciable beam was lost because of this gating system.

7. Scintillation Counters

The counters S were all $\frac{3}{8}$-in. plastic scintillators, 8 in. in diameter. The counters A, B, A', and B' were each composed of 4 separate 13-in.$\times$16-in.$\times\frac{3}{8}$-in. scintillators, with the outputs added as shown in Fig. 5. Counters C and C' have been described as 6 separate counters 2 in. thick, and 25 in.$\times$23 in., connected both into the trigger logic and the hodoscope circuit. The anticoincidence scintillators E and E' were $\frac{3}{4}$ in.$\times$14 in.$\times$14 in. with an 8-in. hole in the center and were centered on the beam line, and D and D' were $\frac{3}{4}$ in.$\times$18 in.$\times$18 in.

8. Hydrogen Targets

The targets were each 54 in. long and 9 in. in diameter (see Fig. 2). The targets proper were made of 0.010-in. Mylar, and were surrounded by 0.19 g/cm² of Mylar and aluminum heat shield. The heat shield and target were contained in a vacuum jacket of 0.62 g/cm² of aluminum. Thus, the total target material outside of the hydrogen volume was 0.82 g/cm² of aluminum and Mylar. Difficulty with the liquid hydrogen "percolating" out the vent was overcome by placing a "dash pot" in the vent line which prevented the liquid from percolating all the way up the vent line.

III. EXPERIMENTAL PROCEDURE AND RESULTS

1. Preliminary Runs, Background Measurement, and Reduction

The early runs of the experiment were primarily devoted to problems of measuring and reducing the pion background in the scattered data. Although the Čerenkov counters should have reduced the pion contamina-
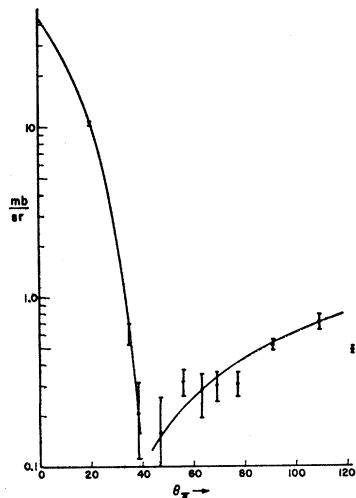
Fig. 7. Differential cross section for elastic $\pi-p$ scattering at 1.16 BeV/c taken from Ref. 15.

Fig. 9. Ratio of pion differential cross section to Rosenbluth cross section shown in Figs. 7 and 8, respectively.

tion to tolerable levels (see Sec. II), in fact, direct measurements showed the contamination was many times too large. Several additional background sources were found and reduced to tolerable levels in these early runs.

Background Measurements

The methods described in Sec. II could not be used to measure pion contaminations of 1 part in 10^6. However, the difference in the angular distributions of elastically scattered pions and muons provided a means of measuring this contamination. In Figs. 7 and 8 are shown the differential elastic scattering cross section for 1.2-BeV/c pions[15] and muons,[16] respectively, and Fig. 9 shows the ratio, $(d\sigma_\pi/d\Omega)/(d\sigma_\mu/d\Omega)$. The muon cross section is seen to drop with increasing angle; but the pion cross
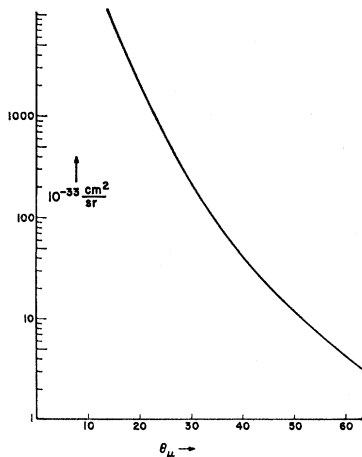

Fig. 8. Differential cross section for elastic electromagnetic scattering at 1.21 BeV/c incident momentum. Calculated from the Rosenbluth cross section using proton form factors given in Ref. 16.
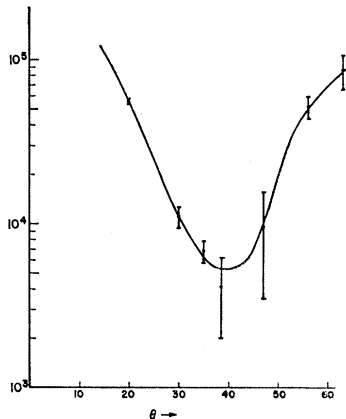
section reaches a minimum at about 50°, and then rises with increasing angle to a maximum at about 110°. Thus, the pions have proportionately many more large angle scatterings. Figure 10 shows the angular distribution obtained in our spark chambers for a pion run (K removed from the trigger). It is seen that there are nearly as many pions in the region 57° to 120° as there are in the region 22° (the minimum accepted angle) to 57°. For the same total number of scattered muons, we would expect no scatterings greater than 50°. Thus, in our muon runs, we assume all scatterings greater than 60° are pions, and limit the region of the muon experiment to the 22°–57° region. (By this procedure, we give up the possibility of finding a large muon anomaly at large angles. This is discussed later.)

Background Sources

The early muon runs gave scattering distributions quite similar to the pion run of Fig. 10, and indicated a pion contamination greater than 30 times the tolerable level. This was traced to the following type of accidental coincidence. A muon would pass through the Čerenkov counters giving the correct K coincidence and, within the resolving time of the electronics (about 30 nsec), a pion would also come down the beam channel and be scattered in the hydrogen target. The anticoincidence
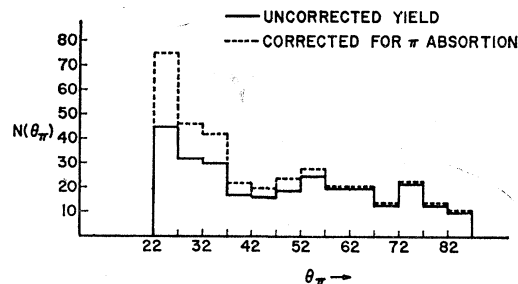

Fig. 10. Experimental angular distribution for elastic pion-proton scattering. These data were obtained from short supplementary runs, throughout the experiment, by removing the K coincidence requirement from T_F or T_B.

[15] C. D. Wood, T. J. Delvin, J. A. Helland, M. J. Lonzo, B. J. Moyer, and Perez-Mendez, Phys. Rev. Letters 6, 481 (1961).

[16] F. Bumiller, M. Criossiaux, E. Dally, and R. Hofstadter, Phys. Rev. 124, 1623 (1961). This is the electron-scattering data which we have converted to a hypothetical muon cross section.
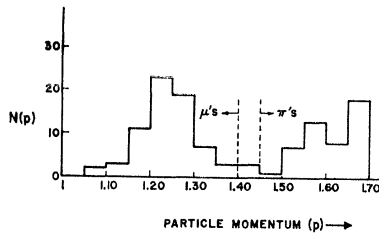
FIG. 11. Momentum distribution of elastically scattered particles. The momenta obtained X_1X_2 pictures is shown. The high-momentum component is due to high-momentum pions that were capable of giving a signal in the Čerenkov counters. The region between 1.40 and 1.45 BeV/c gives rise to a small systematic error, while the muon component is taken between 1.05 and 1.40 BeV/c.

counters D and E were then placed as shown in Fig. 2, where they could intercept the muon and reject this type of event. The anticoincidence arrangement for the back target which eliminated this type of background also included E of the first target. It proved more difficult to discover this contamination, and as a result the back target did not yield as much data as the front target.

Pion contamination in the scattered data also arose from high-energy pions (~ 1.6 BeV/c) which managed to get up the beam channel (probably by scattering from the magnet pole faces, etc.), and because of their high velocity triggered the Čerenkov counters. However, these were easily rejected by the X_1X_2 momentum measurement. In Fig. 11 is shown the momentum distribution of the scattered particles which are seen to divide into two groups—the muons from 1.05–1.40 BeV/c and the high-energy pions from 1.45–1.75 BeV/c.

2. Data Runs

The final data runs occurred after the anticoincidence counters were in place. A total of 3×10^8 muons were incident on both targets (2×10^8 on the front target and 1×10^8 on the back). The spark chambers triggered once in about every 9×10^5 incident muons and the rate of
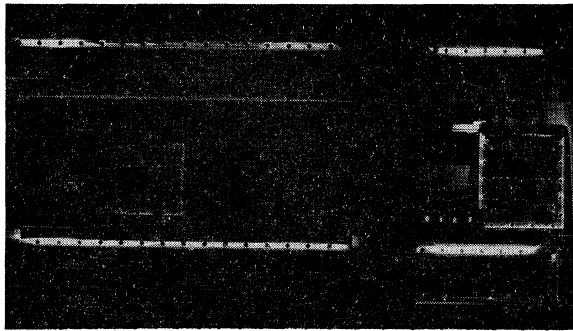

FIG. 12. Typical photograph of an event. This is the picture of the chambers as seen in the example of Fig. 2. The muon is identified by the light which indicates a penetrating particle. Notice that the image of X_3 has been translated midway between X_4 and X_5, while X_8 appears in its true location ahead of the rear target.

good events was about 5 in 10^7 (see below). Some of the additional triggers (aside from the good events) were caused by high-energy pions as mentioned above, but the majority came from unknown sources. About $\frac{1}{4}$ of the pictures showed no tracks in either chamber, and many showed but a single track. Because of the extremely slow trigger rate, it was necessary to intersperse pion runs with muon runs to insure that all parts of the experiment were functioning properly. In addition to the primary data, runs were also made with the incident beam (trigger on SK) to determine its momentum distribution, incident angular distribution, and lateral distribution. The results of these runs are summarized in Table I. Finally, a "target empty" run was made to determine the amount of scattering from the walls.

TABLE I. Values of experimental parameters used in the experiment. Where parameters contribute an error to the experimental yield or a correction to the theoretical yield these errors and corrections are listed in the last column.

Experimental parameter	Value	Correction or error[a,b]
Mean incident muon momentum	1.21 BeV/c	
Spread in incident momenta (including energy loss in targets)	0.07 BeV/c	+0.03
Total incident flux (sum on both targets)	3.0×10^8	
Mean angular spread in incident flux	0.6°	neg
Average vertical angle of incident flux with respect to target axis	0.5°	−0.03
Correction due to knock-on electrons counting in anti's		−0.03
Radiative correction		neg
Error in kinematic selection		±0.03

[a] + sign means that correction increases the "effective" muon flux in the theoretical yield calculation

[b] ± indicates an error which has been combined with the statistical error. Neg means a negligible error.

3. Analysis

Figure 12 is a typical picture of an event as seen by the target-detector camera. The film was first quick-scanned on a Recordak and only those events which showed tracks in both upper and lower chambers and in which the end-view tracks were coplanar to within 15° were accepted for further measurement. This reduced the events from an original 800 to about 500. Measurements were then made on the angles and positions of both tracks (upper and lower chambers) in both views (front and end). The end-view measurements were corrected for the effects of conical projection and mirror rotation; together these gave angular corrections between 0° and 4° depending upon the track orientation. (Thus, in Fig. 12 the apparent uncoplanarity is due in part to these effects.) Corrections of about 0.5° were also applied to remove the optical distortion introduced by the spark-chamber plate reflections (discussed in Sec. II). The total corrections to the front view were of the order of 1° and have been included. All measurements were made using a digitized drafting head which
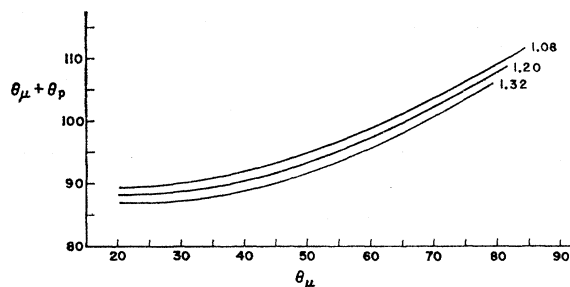
FIG. 13. Kinematic relation of the opening angle $(\theta_\mu+\theta_p)$ for elastic scattering to the muon scattering angle. For these plots the incident momenta were 1.08, 1.20, and 1.32 BeV/c.

entered the angular measurements directly onto an IBM card through a Datex encoder. The rms angular measurement errors were 0.7°.

The corrected measurements were used to calculate the following for each event: the true space angles and positions for the two (upper and lower chambers) tracks, their intersection points (or interaction point), the opening angle θ between the two, and difference angle from coplanarity $\Delta\alpha$. In addition, the momentum of each event was determined from the X_1X_2 film, and then $\Delta\theta$, the difference angle between the measured θ and the correct kinematic opening angle for that momentum and scattering angle, was determined. (Figure 13 gives the kinematic relation between the scattering angle θ_μ and the opening angle $\theta_\mu+\theta_p$ for 1.08, 1.20, and 1.32 BeV/c incoming momenta.)

An acceptable event was first required to have the interaction point within the hydrogen target volume and to have $\Delta\alpha<6°$; this reduced the number of events to 180. Then to separate the muons from the higher momentum pions, the momentum of the incoming particles for each event was plotted, as shown in Fig. 11; only events with incoming particle momentum between 1.05 and 1.40 BeV/c were accepted; this reduced the
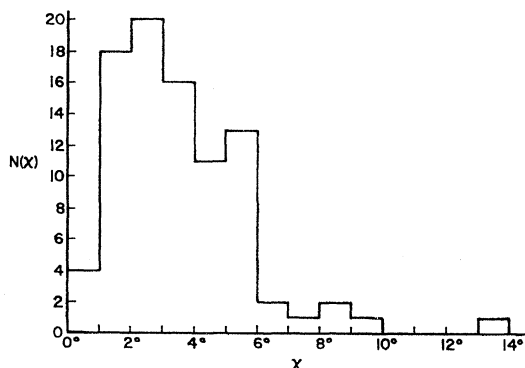

FIG. 14. Angular resolution of kinematics. The quantity $\chi=((\Delta\theta)^2+(\Delta\alpha)^2)^{1/2}$ is the sum of the squares of the angular deviations from correct kinematics of the opening angle $(\theta_\mu+\theta_p)$ and the end view projection, α. Events which did not fulfill all the kinematic criteria to within an rms angle of 6° were considered inelastic. This cutoff gave rise to a possible systematic error of ±2 events.

events to 100 and gave a systematic error of ±4 events (see Table I). Then the requirement $\Delta\theta<10°$ reduced the events to 86. Finally, a plot of the distribution of $\chi\equiv((\Delta\theta)^2+(\Delta\alpha)^2)^{1/2}$, was made, which is shown in Fig. 14, and on the basis of the shape of this curve, only events with $\chi<6°$ were accepted. This accepted range of χ gives the practical resolution of our detector system. The main contributions to the width of χ arise from multiple scattering of the recoil proton, measurement errors and the fact that the end view is not always perpendicular to the incident particle momentum. The events with $\chi>6°$ are presumably inelastic events (see Sec. IV). A systematic error is made in this kinematic selection; we have estimated it to be ±2 events and it has been included in Table I. Thus, those events which were finally selected as candidates for elastic muon scatterings, had momenta between 1.05 and 1.4 BeV/c,
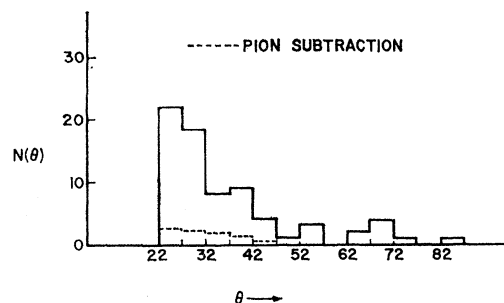

FIG. 15. Experimental angular distribution for elastic scattering events of the muon runs. The events between 22° and 45° are predominantly due to muons, but contain a small pion contamination, shown by the dashed line. Above 56° the events were interpreted to be pions, and together with the distribution shown in Fig. 11 led to the pion subtraction. The small angle cutoff is taken at 22° in order to avoid large systematic errors due to the sensitivity of the calculated efficiency at small angles to small variations of the geometry.

$\chi<6°$, and their interaction point lay within the target volume. Eighty events were left, and their angular distribution is plotted in Fig. 15. We now apply our assumption that any scatterings greater than 56° are pions (see Sec. II) thus with this criterion there are 9 pions greater than 56°. The experimental pion distribution of Fig. 10 can now be used to calculate the expected number of pions in the angular region between 22° and 56°. These are given in Table II in the last column. Hence, the final experimental muon distribution, including pion subtraction, is given in column two of Table II.

IV. THEORETICAL YIELD

The most convenient way to relate the above observed scattering distribution to the cross section is to calculate the expected theoretical yield. This was done from the following expression for the differential yield at a muon angle θ_μ:

$$[\Delta Y(\theta_\mu)/\Delta\theta_\mu]=N_0\rho\,\sin\theta_\mu[d\sigma(\theta_\mu)/d\Omega]N_\mu[2\pi l\eta(\theta_\mu)],$$

TABLE II. Experimental and calculated yields for the experiment. The experimental yield has been corrected for pion contamination and also includes the systematic errors mentioned in Table I. The errors in the calculated yield arise from geometric uncertainties and are negligible for angles greater than 32°. The calculated yield also includes the corrections listed in Table I. The amount of pion background subtracted from the experimental yield is given in the last column.

Lab angle interval (deg)	Corrected experimental yield	Calculated yield	π background
22–26.9	21.3±5.8	18.1±0.9	2.7±1.0
27–31.0	15.8±4.9	13.4±0.3	2.2±0.8
32–36.9	6.2±3.2	8.5	1.8±0.7
37–41.9	8.8±3.5	5.0	1.2±0.5
42–46.9	3.4±2.1	2.9	0.6±0.3
greater than 47 (assumed π's)	9.0±3.0		

where N_0 is Avogardo's number, ρ is the density of liquid hydrogen, l is the length of the target, N_μ is total muon flux, and $\langle d\sigma(\theta_\mu)/d\Omega \rangle_{av}$ is the average over $\Delta\theta$ of the theoretical Rosenbluth cross section with the experimental electron-proton form factors[17] $F_1(q^2)$ and $F_2(q^2)$ given by Hofstadter.[16] $\eta(\theta_\mu)$ is the detector efficiency and is calculated from the expression

$$\eta(\theta_\mu) = \int \int \int \int dx\,dy\,dz\,d\varphi/2\pi lA \;,$$

where x, y, and z are the rectangular coordinates of a point within the target volume (x is in the beam direction), A is the cross-sectional area of the target, and ϕ is the azimuthal angle of scattering. The quadruple integral is to be carried out over values of ϕ which include the detectors (either spark chambers or triggering scintillators) from each point within the target and these integrated over the target volume. $\eta(\theta_\mu)$ was evaluated with the aid of the IBM-709 computer, the results are given in Fig. 16.

The uncertainty in $\eta(\theta_\mu)$ caused by the estimated uncertainty in the location of the detector was also calculated and was found to be large at the very small angles ($<22°$). Thus, the data was restricted to angles greater than 22°. The errors given in Table I to the theoretical yield were obtained from these considerations and are only significant up to 32°. Uncertainties in $\eta(\theta_\mu)$ were also calculated for the known uncertainties in our beam parameters (e.g., mean incident angle with respect to the target axis) and found to be negligible. The other systematic errors or corrections are summarized in Table I.

[17] K. J. Barnes, Nuovo Cimento **27**, 228 (1963). The probable error in the Rosenbluth cross section due to the neglect of terms which include the muon mass was estimated for this experiment and found to be negligible. For the most unfavorable conditions of the experiment ($q^2 \approx 16$ F^{-2}) which constitutes a very small part of the data, the effect of the muon mass on the predicted yield cannot be greater than 5%; for the bulk of the data ($q^2 \sim 12.5$ F^{-2}) it cannot be greater than 3%.
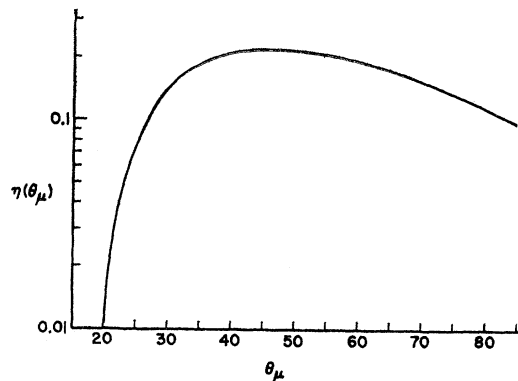

FIG. 16. Geometrical efficiency of scattering detectors versus scattering angle. Above 22° the efficiency is quite insensitive to small variations in the geometry, and hence, leads to very small systematic errors in the final results.

V. DISCUSSION

The final distribution of the scattered events is given in Fig. 15. As has been mentioned earlier, we have forced the following interpretation of this distribution: events for $\theta > 60°$ are pions and events for $22° < \theta < 45°$ are predominantly muons with a 9% pion background, the background having been calculated from the measured angular distribution of pure pions (Fig. 10) and the assumed pions for $\theta > 60°$. A measure of the validity of this interpretation is obtained by comparing the ratio of large to small angle events for the pion and muon runs. That ratio for the muons is seven standard deviations away from the one obtained in the pion runs. Thus, it is clear that the scattered events for $22° < \theta < 60°$ are predominately muons. Although we cannot, strictly speaking, prove that the events for which $\theta > 60°$ are pions, there are several indications that this interpretation is correct. The angular distribution for these events agrees with the measured distribution of pions in that region (see Fig. 10). In addition, any relaxation of the pion rejection criteria, such as removing a single Čerenkov counter, or removing part of the anticoincidence system, increased the number of events for $\theta > 60°$ relative to those for $22° < \theta < 60°$. It should be noted that this interpretation does eliminate the possibility of observing a large muon anomaly at very large momentum transfers ($q^2 > 16$ F^{-2}), but such an anomaly would have to be ~ 100 times the theoretical cross section if those events (for $\theta > 60°$) were, in fact, muons. This, together with the behavior of these events, as noted above, makes their interpretation as pions quite convincing.

Figure 14 gives the accuracy with which the measured angles, θ and α, of the event fit the kinematically correct angles for elastic muon scattering. As mentioned in Sec. III, we have selected as elastic scatterings only those events for which $\chi < 6°$. Those events for which $\chi > 6°$ are presumably inelastic events, either pions or muons. It is interesting to note that the number of

these events is compatible with the number of inelastic muons expected from theoretical calculations.[18]

In Fig. 17 the final experimental yield, $(dY/dq^2)_{\text{exp}}$, is compared with the expected theoretical yield, $(dY/dq^2)_{\text{theo}}$, by forming the ratio

$$R = (dY/dq^2)_{\text{exp}}/(dY/dq^2)_{\text{theo}}$$

and plotting versus q^2. A χ-square analysis gives a 75% confidence level that the experimental points agree with the value $R=1$ and, hence, that our data is in agreement with the expected electromagnetic cross section. This is the primary conclusion from this experiment.

We may also examine to what extent this experiment puts a limit on a possible muon-electron difference. This may be formulated quantitatively by adopting a model for this difference, and within the limitation of this model we may also make comparisons with other experiments which might observe muon-electron differences. The conventional model[9] assumes that quantum electrodynamics breaks down for the muon vertex at some small distance which is characterized by the quantity Λ^{-1}, and that this breakdown alters the Rosenbluth cross section in multiplying it by the factor $f_\mu(q^2,\Lambda)$ $= (1-2q^2/\Lambda^2)$. We may give a physical interpretation to the breakdown at the muon vertex by assuming that the muon's charge has a finite distribution. This will lead to replacing, in the Rosenbluth cross section, the form factors F_1 and F_2 due to the proton vertex, with the product form factors $F_1F_{\mu 1}$ and $F_2F_{\mu 2}$, due to both proton and muon vertices.[19,20] If we further assume that $F_{\mu 1}=F_{\mu 2}$, then $F_{\mu 1}$ can be written, $F_{\mu 1}=1-\frac{1}{6}\langle r_\mu^2\rangle^{1/2}$ where $\langle r_\mu^2\rangle^{1/2}$ is the rms radius of the muon's charge distribution, and we then see that $f_\mu=F_{\mu 1}^2$ with $\langle r_\mu^2\rangle^{1/2}=6^{1/2}\Lambda^{-1}$. One should remember that there are other interpretations to Λ within this model, and there are certainly other models which might be con-
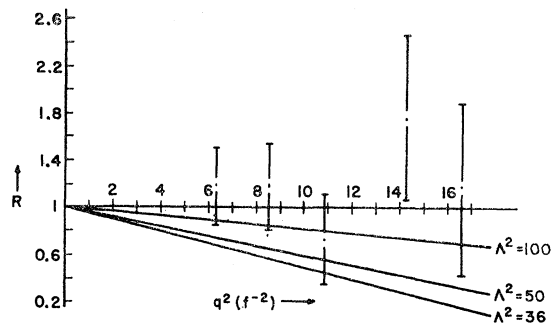

FIG. 17. Ratio of Experimental $\mu - p$ cross section to Rosenbluth cross section. The ratio is interpreted as a form factor which is also plotted on the graph for several values of Λ^2. A χ^2 analysis gives at the 95% confidence level $\Lambda^{-1}<0.16$ F.

sidered for a muon-electron difference. But keeping to this model, we may now ask: What is the upper limit which this experiment places on Λ^{-1}; or using the charge distribution interpretation of Λ^{-1}: What is the largest muon-charge distribution compatible with the results of this experiment. In Fig. 17 we have also plotted $(d\sigma/dq^2)_{\text{mod}}/(d\sigma/dq^2)_{\text{Ros}}=f_\mu(q^2,\Lambda)$, for various Λ, where $(d\sigma/dq^2)_{\text{Ros}}$ is the Rosenbluth cross section and $(d\sigma/dq^2)_{\text{mod}}$ is the same cross section modified by the factor f_μ. A χ-square analysis comparing the experimental points with the curves for various Λ gives, with 95% confidence, $\Lambda^{-1}<0.16$ F for a positive Λ^2. If we lift the restriction that Λ^2 be positive, the best fit to the data is found for a negative Λ^2 and $\Lambda^{-1}=(0.07\pm0.1)$ F. Comparable numbers from other experiments are as follows: The CERN scattering experiment gives $\Lambda^{-1}<0.28$ F (95%); the $g-2$ experiment considering only the muon vertex gives 0.17 F (95%).

ACKNOWLEDGMENT

---

[18] The theoretical cross section used to calculate the yield of inelastic scattering was provided by S. Berman (private communication).

[19] S. D. Drell and F. Zachariasen, *Electromagnetic Structure of Nucleons* (Oxford University Press, London, 1961), pp. 88–96.

[20] It should be noted that the measured form factors F_1 and F_2 from electron-proton scattering may actually be product form factors due to form factors at the electron and proton vertices. The electron-proton experiments cannot separate the two vertex effects, and it will be necessary to wait for other experiments (e.g., electron-electron scatterings at high q^2) to unravel them. Hence, the F_μ above is intended to be a "difference" form factor between muon and electron vertices.
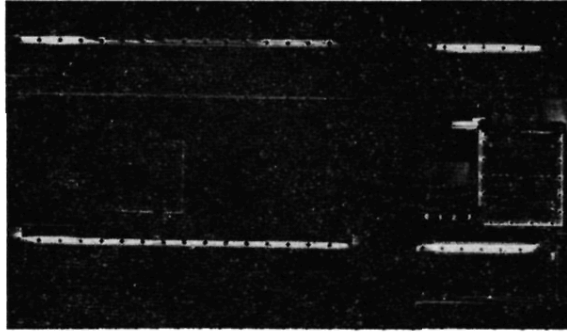
FIG. 12. Typical photograph of an event. This is the picture of the chambers as seen in the example of Fig. 2. The muon is identified by the light which indicates a penetrating particle. Notice that the image of X_3 has been translated midway between X_4 and X_5, while X_8 appears in its true location ahead of the rear target.
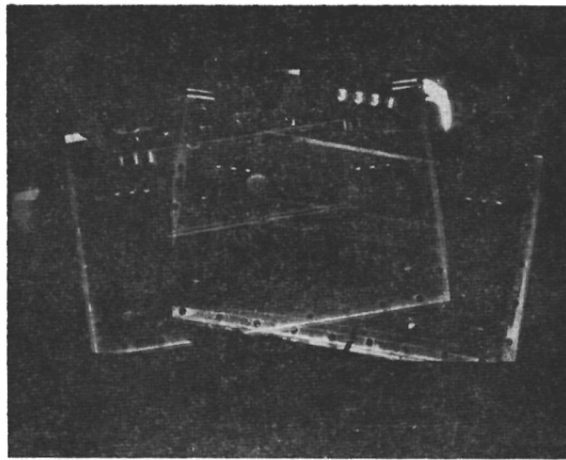
FIG. 3. Momentum defining photograph. A typical photograph of the X_1X_2 tracks superimposed on a single frame is shown. The angular difference between the two tracks uniquely defines the momentum for any fixed current setting of the bending magnet.